Nanoscale

REVIEW

View Article Online
View Journal | View Issue

Cite this: *Nanoscale*, 2020, **12**, 22891

Rich information on 2D materials revealed by optical second harmonic generation

He Ma,[a] Jing Liang,[a] Hao Hong,[a,b] Kehai Liu,[c] Dingxin Zou,[d] Muhong Wu[e] and Kaihui Liu *[a,f]

Received 19th August 2020,
Accepted 19th October 2020

DOI: 10.1039/d0nr06051h

rsc.li/nanoscale

Two-dimensional (2D) materials have brought a spectacular revolution in fundamental research and industrial applications due to their unique physical properties of atomically thin thickness, strong light–matter interaction, unity valley polarization and enhanced many-body interactions. To fully explore their exotic physical properties and facilitate potential applications in electronics and optoelectronics, an effective and versatile characterization method is highly demanded. Among the many methods of characterization, optical second harmonic generation (SHG) has attracted broad attention because of its sensitivity, versatility and simplicity. The SHG technique is sufficiently sensitive at the atomic scale and therefore suitable for studies on 2D materials. More importantly, it has the capacity to acquire abundant information ranging from crystallographic, and electronic, to magnetic properties in various 2D materials due to its sensitivity to both spatial-inversion symmetry and time-reversal symmetry. These advantages accompanied by its characteristics of non-invasion and high throughput make SHG a powerful tool for 2D materials. This review summarizes recent experimental developments of SHG applications in 2D materials and also provides an outlook of potential prospects based on SHG.

1. Introduction

Second harmonic generation (SHG) is the most fundamental process in nonlinear optics and gives rise to radiation at twice the frequency of the incident light.[1–20] Since observed by Franken in a quartz crystal in 1961, SHG has been an important characterization method in many fields of science such as physics, surface chemistry and bio-imaging.[1–4] The SHG signal of a medium can originate from different types of polarization, which mainly include electric dipole (ED), electric quadrupole (EQ) and magnetic dipole (MD), encoding the underlying information of the crystallographic, electronic, and magnetic structure of crystalline materials.[3,5] Since the dominant ED polarization is extremely sensitive to symmetry variations and only allowed in noncentrosymmetric materials, it is widely used in noncentrosymmetric media such as ferroelectric/piezoelectric crystals, surface and interface characterization, and especially at the interface of two adjacent centrosymmetric bulk materials.[6–8] Although the EQ and MD contributions are usually much weaker than the ED contribution in noncentrosymmetric materials, they are able to exist in a centrosymmetric medium where the ED contribution vanishes and provide abundant information on the medium.[9–12] SHG also shows the ability to uncover magnetic order in magnetically ordered materials, even the hardly detectable antiferromagnetic order which lacks net macroscopic magnetization.[13] In addition, when combined with time-resolved spectroscopy, SHG is capable of capturing ultrafast temporal evolution related to broken symmetry such as ultrafast phase transition induced by a femtosecond laser.[14–16]

The emerging two-dimensional (2D) family consists of a wide range of materials, ranging from gapless graphene, insulating hexagonal boron nitride (h-BN) to magnetic CrI_3, attracting great interest due to their distinctive properties and great potential for novel applications.[17–19] The atomically thin nature of 2D materials reduces the dielectric screening and enhances Coulomb interactions, which leads to unique electronic and optical properties.[20–22] In the meantime, however, atomically thin thickness also adds great difficulties in revealing the basic structure and novel properties when utilizing conventional techniques such as X-ray diffraction (XRD), transmission electron microscopy (TEM), *etc*.[23–25] Inevitably time-consuming data acquisition processes and sophisticated

[a]*State Key Laboratory for Mesoscopic Physics, Collaborative Innovation Center of Quantum Matter, Academy for Advanced Interdisciplinary Studies, School of Physics, Peking University, Beijing, 100871, China. E-mail: khliu@pku.edu.cn*
[b]*Huairou National Comprehensive Science Center, Beijing, 100871, China*
[c]*Songshan Lake Materials Laboratory, Institute of Physics, Chinese Academy of Sciences, Guangdong, 523808, China*
[d]*Shenzhen Institute for Quantum Science and Engineering, Department of Physics, Southern University of Science and Technology, Shenzhen, 518000, China*
[e]*International Center for Quantum Materials, Collaborative Innovation Center of Quantum Matter, Peking University, Beijing, 100871, China*
[f]*Frontiers Science Center for Nano-optoelectronics, Peking University, Beijing, 100871, China*

sample treatments call for a more simple method to study 2D materials. Some practical techniques for bulk materials such as neutron diffraction are even invalid at the 2D limit. As a non-invasive and high-throughput optical method, SHG meets the urgent characterization need for 2D materials and provides an excellent platform for acquiring information about the crystallographic, electronic, and magnetic properties of 2D materials.[26] The extreme sensitivity to both spatial-inversion symmetry and time-reversal symmetry of SHG can be of great use in revealing many symmetry-related phenomena such as crystal symmetry, phase transition and magnetic order.

In this review, we survey recent progress of SHG applications in 2D materials, extending from electric-dipole approximation to multipole approximation. We first briefly describe the physical mechanisms that underlie the different origins of SHG in materials. Then, we mainly focus on five aspects of SHG applied in 2D materials, *i.e.* crystal structure characterization, strain tensor visualization, phase transition, electron–hole symmetry and antiferromagnetic (AF) order detection (Fig. 1). Large enhancement and tunability of SHG modulated by exciton resonance and integrated with nanophotonics is also discussed. Finally, we present a perspective of potential research topics of order parameters and fine structure distortion based on SHG spectroscopy.

2. Background of SHG

The nonlinear process SHG can be expressed as $P(2\omega = \omega + \omega) = \chi^{(2)}{:}E(\omega)E(\omega)$, where $\chi^{(2)}$ is a three-rank nonlinear susceptibility tensor. In the case of multipole approximation,

$$\chi^{(2)}(\omega, \mathbf{q}) \approx \chi^{(2)}_{\mathrm{ED}}(\omega) + \chi^{(3)}_{\mathrm{EQ}}(\omega)\mathbf{q} + o(\mathbf{q}^2) \quad (1)$$

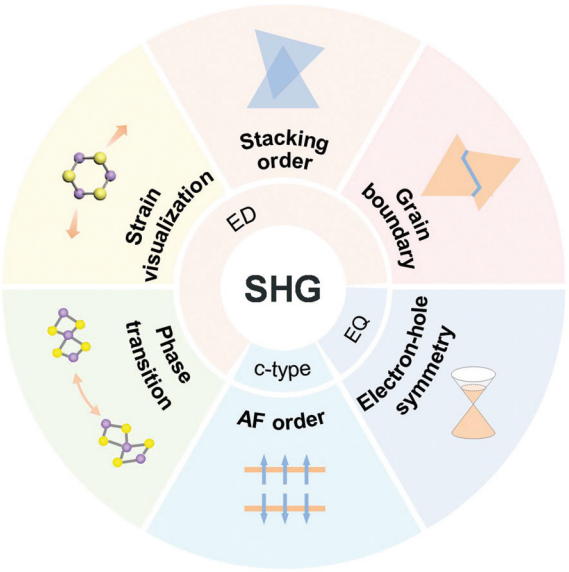

Fig. 1 Schematic illustration of the properties of 2D materials revealed by SHG and the corresponding mechanisms.

where ω and $\mathbf{q}$ are the incident frequency and photon wave vector, respectively.[27] The three-rank tensor $\chi^{(2)}_{\mathrm{ED}}(\omega)$ is the ED term and leads the strongest contribution in $\chi^{(2)}$. The four-rank tensor $\chi^{(3)}_{\mathrm{EQ}}(\omega)$ is the contribution of the EQ. $\chi^{(2)}_{\mathrm{ED}}$ is constrained not only by the formal symmetry properties of the tensor itself but also by the symmetry of the nonlinear media. The natural symmetries of $\chi^{(2)}_{\mathrm{ED}}$ consist of intrinsic permutation symmetry, full permutation symmetry and Kleinman's symmetry.[122] By imposing these restrictions, 27 Cartesian components in the three-rank tensor $\chi^{(2)}_{\mathrm{ED}}$ are simplified into 10 independent elements. When considering crystallographic contribution, the spatial symmetry of a medium requires itself to keep identical after the crystal symmetry operation, and this further confines the independence of components in $\chi^{(2)}_{\mathrm{ED}}$. One typical symmetry characteristic is inversion symmetry, the determinant of whose operation is $\hat{I} = \begin{pmatrix} -1 & 0 & 0 \\ 0 & -1 & 0 \\ 0 & 0 & -1 \end{pmatrix}$. If the medium hosts inversion symmetry, components in $\chi^{(2)}_{\mathrm{ED}}$ will follow the relation $\chi^{\mathrm{ED}}_{ijk} = -\chi^{\mathrm{ED}}_{ijk}$, which finally leads to $\chi^{\mathrm{ED}}_{ijk} = 0$. Therefore, $\chi^{(2)}_{\mathrm{ED}}$ vanishes in the centrosymmetric medium and ED-SHG is extremely sensitive to crystallographic inversion symmetry. In the non-centrosymmetric medium, the ED-SHG signal can provide abundant information associated with crystallographic symmetry such as lattice structure and crystal orientation.

In centrosymmetric systems, ED-SHG is forbidden and SHG can only arise from higher-order multipole contributions such as EQ-SHG. This kind of signal is pretty weak in the presence of ED-SHG, but some centrosymmetric media can generate an appreciable EQ-SHG signal when it is linked to electronic transitions.

For magnetically ordered materials, $\chi^{(2)}$ can be given by

$$\chi^{(2)} = \varepsilon_0(\chi^{(\mathrm{i})} + \chi^{(\mathrm{c})}) \quad (2)$$

The i-type tensor $\chi^{(\mathrm{i})}$ and c-type tensor $\chi^{(\mathrm{c})}$ are responsible for crystallographic and magnetic structure contributions to SHG, respectively.[3] In general, tensors can be divided into two types: i-type if they are invariant under the time reversal operation and c-type if they change the sign under temporal inversion. Thus, c-type contributions are only allowed when magnetic order exists. Besides MD contribution, magnetic order can also generate ED-SHG. Since a noncentrosymmetric magnetic order breaks both spatial-inversion symmetry and time-reversal symmetry, this kind of SHG is denoted as c-type ED-SHG.

3. Crystal structure symmetry

Atoms in crystalline solids are arranged in periodic patterns which can be characterized by different sorts of symmetries.[121] Crystal symmetry plays an important role in governing the fundamental physical properties of materials, so the crucial task

of a 2D material study is to identify crystal symmetry. Compared with traditional XRD and TEM techniques, SHG is a more rapid and versatile way to study 2D materials without sophisticated sample treatments. Since the leading term $\chi^{(2)}_{ED}$ in the SHG signal is encoded with the spatial symmetry of the medium, the widest application of SHG is crystal symmetry characterization. For example, the widely studied monolayer MoS_2 and h-BN both lack crystal inversion symmetry and exhibit strong intrinsic SHG signals.[28–30] Monolayer MoS_2 and h-BN both belong to the D_{3h} point group with in-plane three-fold rotational symmetry. The parallel and perpendicular components of polarization-dependent SHG can be represented as $I_{\parallel} = I\cos^2(3\theta)$ and $I_{\perp} = I\sin^2(3\theta)$, respectively, where θ is the angle between the excitation laser polarization and crystalline armchair direction (Fig. 2a). Such polarization-dependence of SHG is consistent with the in-plane three-fold rotational symmetry. Therefore, the rotational anisotropy of the SHG pattern has one-to-one correspondence with the crystallographic orientation of MoS_2/h-BN, that is, the maximum intensity in the parallel component of polarized SHG indicates the armchair direction of MoS_2/h-BN.

Grain boundaries are also a basic issue for crystals. The atomic edge may host exotic electronic and optical properties completely different from the domain inside. Particularly for 2D materials, studying the grain boundary is of great importance driven by the urgent need for growth of large area single crystals since it is key to unveiling the mechanism of epitaxial growth and formation of grain boundary.[31,32] The one-dimensional (1D) atomic boundary inside the materials is hard to detect. Just as shown in Fig. 2b, the grain boundary of the polycrystalline monolayer MoS_2 is totally invisible in the optical image.[33] In contrast, SHG is a great choice for grain boundary visualization due to its sensitivity to symmetry variations. Adjacent grains with different orientations lead to destructive interference and annihilation at boundaries, hence the grain boundaries inside appear as narrow dark lines on SHG images. In addition, SHG resonance at about 1310 nm is observed on the atomic edges of monolayer MoS_2.[34] Nonlinear optical susceptibility is significantly enhanced when the real energy level is in the vicinity of virtual states that are involved in the nonlinear optical process as density of states dramatically increase.[35–37] Since the photon energy of 1310 nm isn't consistent with A-exciton of monolayer MoS_2, this resonance of the optical nonlinear response is eventually attributed to the 1D edge states of monolayer MoS_2. In addition, the *in situ* SHG study of chemical vapor deposition (CVD) growth of MoS_2 reveals that the grain boundaries of polycrystalline monolayer MoS_2 are peculiarly prone to be polylines with 120° tuning angles instead of direct straight lines between intersecting corners, which is also reasonable from the perspective of the three-fold rotational symmetry of the MoS_2 lattice.[33]

Apart from single materials, the atomically thin 2D layers can stack into van der Waals heterostructures just like atomic-scale Lego blocks.[38] Such heterostructures generate a new material system and provide infinite possibilities. The same material composition with different stacking sequences and angles leads to totally different physical properties of heterostructures. For instance, graphene trilayers with ABA (Bernal) and ABC (rhombohedral) host different electronic nature: ABA trilayers are gapless semimetals, while ABC trilayers are semiconductors with two nearly flat bands across a gate-tunable bandgap.[39–41] Similarly, the band structure and optical pro-

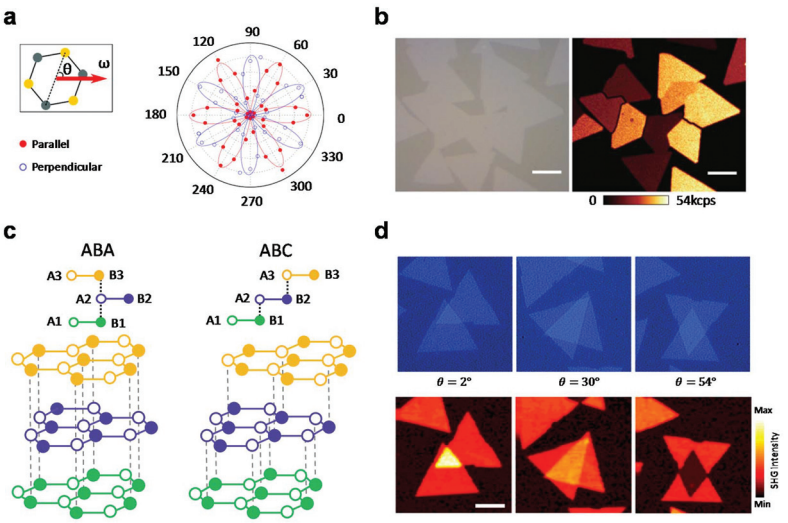

Fig. 2 Crystal structure identification of 2D materials by SHG. (a) Polar plot of angular dependence of SHG intensity from a monolayer MoS_2. The red and blue patterns respectively show parallel and perpendicular components of the SHG signal. Reproduced from ref. 28 with permission from American Chemical Society, copyright 2013. (b) Optical and SHG image of a CVD-grown polycrystalline monolayer MoS_2. Reproduced from ref. 33 with permission from Wiley, copyright 2015. (c) Schematic diagram of top (yellow), middle (purple), and bottom (green) layers stacking in the ABA (Bernal) and ABC (rhombohedral) graphene trilayer. A and B are two equivalent atoms in the graphene unit cell. (d) Optical (up) and corresponding SHG mapping (down) images of MoS_2 bilayers with different stacking angles of θ = 2°, 30° and 54°. Reproduced from ref. 46 with permission from American Chemical Society, copyright 2014.

perties of twisted bilayer MoS_2 obviously vary with the twisted angle.[42,43] Thus, it is of great importance to identify and precisely control the interlayer stacking structures of heterostrctures.[44]

Graphene trilayers can exist in two stable crystallographic configurations by nature, ABA and ABC stacking order. The flat bands in ABC trilayers are supposed to be promising in superconductivity studies, so it's necessary to distinguish two stacking orders. Differences in stacking orders lead to distinct structural symmetries. The unit cell of graphene's hexagonal lattice contains two inequivalent atoms, A and B. In the ABA trilayer, the B-atoms in the second layer are on top of the centers of the hexagons of the first layer, and the third layer is exactly above the first layer. In the ABC trilayer, each layer is shifted by the distance of an atom from the former layer (Fig. 2c). Thus, the ABA trilayer is noncentrosymmetric and ABC is centrosymmetric. As a result, the ABA trilayer generates an appreciable SHG signal and no evident SHG response can be observed from the ABC trilayer.[45]

As to stacking angle, the SHG field of twisted transition metal dichalcogenide (TMDC) bilayers can be regarded as coherent superposition of individual layers.[46] The total SHG intensity of the twisted bilayer I_s can be expressed as:

$$I_s(\theta) = I_t + I_b + 2\sqrt{I_t I_b}\cos 3\theta \quad (3)$$

I_t and I_b are the SHG signals originating from the top layer and the bottom layer of the twisted bilayer, θ is the stacking angle defined as the angle between two nearest perpendicular bisectors of the two layers. Apparently, the total SHG intensity varies with the stacking angle and is a sensitive criterion for determining the stacking angle in twisted heterostructures (Fig. 2d).

4. Strain visualization

Benefiting from the ultra-strength and ultra-flexibility of 2D materials, strain engineering has been an effective and invertible tool to continuously tune the properties of 2D materials (Fig. 3a).[47–50] Owing to the larger exposed surface area of atomically thin layers, 2D materials are more sensitive to external modulation compared with three-dimensional bulk materials. As a result, the residual strain arising from mismatch during the growth process and the local strain caused by fabrication processes also strongly affect the electronic and optical properties of 2D materials.[35,51] Thus, it is essential to figure out the strain tensor distribution in 2D materials. The direct impact of strain on 2D materials is lattice deformation and symmetry variations. The tensor nature of second-order nonlinear susceptibility $\chi^{(2)}_{ijk}$ enables itself sensitive to crystallographic symmetry, which therefore gives rise to the capacity of monitoring the strain tensor. Compared with the PL method, the nonlinear characteristic of SHG facilities to gain higher spatial resolution, which is vital for the measurement of the local strain in the micro-area. Furthermore, SHG intensity also exhibits high strain-sensitivity, which is almost one order of magnitude larger than that of the PL peak shift.[52]

The applied strain deforms the crystal symmetry and further influences the second order nonlinear susceptibility. The second order nonlinear susceptibility before $\left(\overleftrightarrow{\chi}^{(2)}_b\right)$ and after $\left(\overleftrightarrow{\chi}^{(2)}_a\right)$ strain applied are connected by a linear strain dependence:

$$\overleftrightarrow{\chi}^{(2)}_a = \overleftrightarrow{\chi}^{(2)}_b + \overleftrightarrow{p}\overleftrightarrow{u} \quad (4)$$

where $\overleftrightarrow{p}$ is the photoelastic tensor and $\overleftrightarrow{u}$ is the strain tensor. $\overleftrightarrow{\chi}^{(2)}_b$ is only associated with intrinsic symmetry properties which can be considered already known. Since the strain tensor of the uniaxial tensile strain is symmetric, simultaneously considering crystal symmetry, there will be only several free parameters in the photoelastic tensor. These parameters in $\overleftrightarrow{p}$ and $\overleftrightarrow{\chi}^{(2)}_a$ can be obtained by applying different levels of uniaxial strain combined with polarization resolved SHG signals, and finally the strain tensor is accessed. For intrinsic monolayer $MoSe_2$ with three-fold rotational symmetry, supposing incident light with a certain polarization direction, as mentioned before, parallel ($I_\parallel$) and perpendicular ($I_\perp$) components of the total output SHG signal (I) is $I_\parallel = I\cos^2(3\theta)$ and $I_\perp = I\sin^2(3\theta)$, respectively, where θ is the angle between the excitation laser polarization and crystalline armchair direction. So, the total SHG signal $I = I_\parallel + I_\perp$ and is independent of θ. The parallel and perpendicular components of the polarization dependent pattern $MoSe_2$ are both six petals of the same size, the same as monolayer MoS_2 mentioned before. When uniaxial tensile strain (ε_a along the crystalline armchair direction or ε_z along the crystalline zigzag direction) is applied, the second-order susceptibility tensor changes from the three-fold D_{3h} symmetry into the C_{2v} symmetry. The parallel $\left(I^{(C_{2v})}_\parallel\right)$ and perpendicular $\left(I^{(C_{2v})}_\perp\right)$ polarized components of polarization dependent SHG patterns under ε_a turn into the following:

$$I^{(C_{2v})}_\parallel = \left|d^{D_{3h}}_{22}\left(\cos 3\theta + \varepsilon_a\left(a_1\cos^3\theta - b_1\sin^3\theta\cos\theta - 2c_1\sin^3\theta\cos\theta\right)\right)\right|^2 \quad (5)$$

$$I^{(C_{2v})}_\perp = \left|d^{D_{3h}}_{22}\left(\sin 3\theta + \varepsilon_a\left(a_1\sin\theta\cos^2\theta - b_1\sin^3\theta + 2c_1\sin\theta\cos^2\theta\right)\right)\right|^2 \quad (6)$$

where a_1, b_1, and c_1 are the relative changes of different tensor elements caused by strain perturbation in $\overleftrightarrow{\chi}^{(2)}_a$, which vary with different angles of applied strain, just as shown in Fig. 3b and c. Now, $I = I_\parallel + I_\perp$ is no longer independent of θ but changes dramatically with strain angle and amplitude, as shown in Fig. 3d.

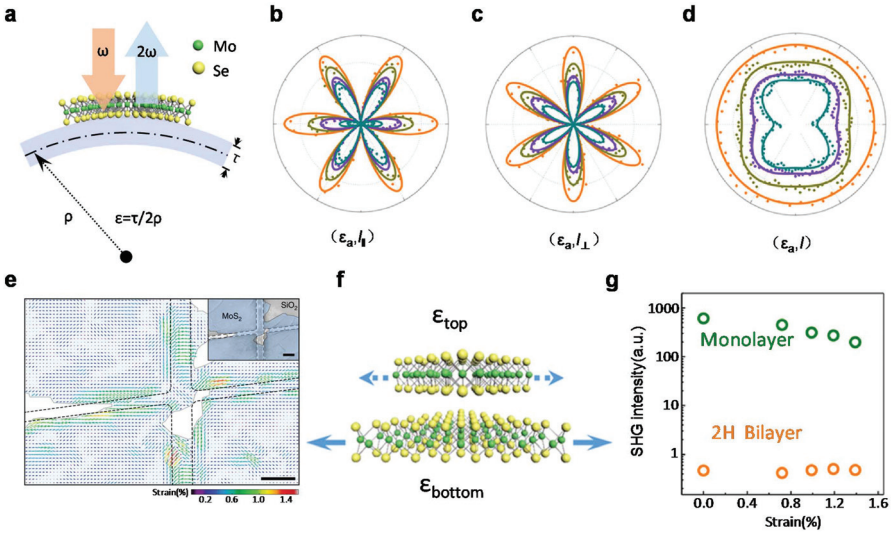

Fig. 3 Strain tensor visualization in 2D materials by SHG. (a) Schematic diagram of the strain apparatus and SHG process in monolayer $MoSe_2$ under uniaxial tensile strain. (b–d) Parallel (b) and perpendicular (c) components of polarization resolved SHG intensity and the total (d) SHG intensity patterns under different strain amplitudes of ε_a which is along the $MoSe_2$ crystalline armchair direction. (e) Strain tensor mapping of MoS_2 monolayer flake (filled color) on a lithographically defined structure (dashed lines). Inset is the SEM image of the same area. (f) Schematic diagram of interlayer strain transfer in 2H bilayer $MoSe_2$. (g) Log-plot of SHG intensity of monolayer and 2H bilayer $MoSe_2$ under different strain amplitudes. (a–d, f–g) Reproduced from ref. 52 with permission from American Chemical Society, copyright 2017. (e) Reproduced from ref. 53 with permission from Springer Nature, copyright 2018.

The applied uniaxial tensile strain clearly alters the shape and intensity of polarization dependent SHG patterns from which parameters in the photoelastic tensor as well as the strain tensor can be extracted by quantitative analysis. Based on this, it is convenient to visualize the strain field of a certain area combined with the SHG mapping technique.[53] The inset of Fig. 3e shows the scanning electron microscopy (SEM) image of the MoS_2 monolayer lying on a lithographically defined structure. The MoS_2 membrane obviously undergoes inhomogeneous strain tensor distribution across the grids. Fig. 3e shows the strain map plot by vectors through the SHG mapping technique, which illustrates the strain distribution clearly and directly.

The requirement of effective strain engineering is noninvasive and reversible. For monolayer 2D materials, this means attention ought to be paid to avoid material rupture when strain is applied. As to heterostructures, criteria become more complicated since undesirable interlayer sliding occurs before the rupture. The SHG experiment proves that 2H $MoSe_2$ bilayers can at least withstand 1.4% relative interlayer strain.[52] 2H $MoSe_2$ bilayers exhibit the centrosymmetric D_{3h} point group and the interlayer sliding will lead to an unequable change in the top and bottom layer and break the inversion symmetry (Fig. 3f), so the sliding can be accessed by the emergence of the SHG signal. In the experiment, SHG intensity can still be neglected even when the strain is up to 1.4% (Fig. 3g). The first principles calculations of the competition between interlayer interaction energy and total strain energy theoretically support experiment results. The van der Waals coupling between adjacent layers is able to make two layers remain locked under percentage level strain.

5. Phase transition

Phase transition is an important constituent of condensed matter systems. Just like ice melting and water boiling, phase transition is the transition between a well-ordered state and a more chaotic phase of matter, and thus broken symmetry is ubiquitous during phase transition. At the atomic scale, phase transitions become richer and more attractive leading to a number of intriguing physical phenomena in 2D materials such as charge density wave transition in TaS_2, superconducting transition in $NbSe_2$ and ferromagnetic transition in $Cr_2Ge_2Te_6$.[54–56] On the other hand, observation of such microscopic transition is rather difficult compared with the macroscopic scale, and it is even harder to straightforwardly probe the underlying symmetry change. SHG apparently has an advantage in identifying the symmetry change in phase transition given its high efficiency in crystal symmetry determination. The symmetry change will give rise to a discontinuous increase or a reduction in SHG intensity. In turn, the variation of SHG intensity is also a proof of the occurrence of phase transition. For instance, $MoTe_2$ and WTe_2 can exist in several different crystal structures with diverse properties. As shown in Fig. 4a, they are trigonal prismatic coordinated 2H phase, distorted octahedral 1T′ phase, and orthorhombic T_d phase.[57–59,123] Among these phases, 2H and T_d phases are noncentrosymmetric and the 1T′ phase is centrosymmetric. It is theoretically proved that the energy difference between the phases of $MoTe_2$ is small.[60] As a result, phase transition in $MoTe_2$ can be induced in many ways such as electrostatic doping and laser irradiation. In the electrostatic doping experi-

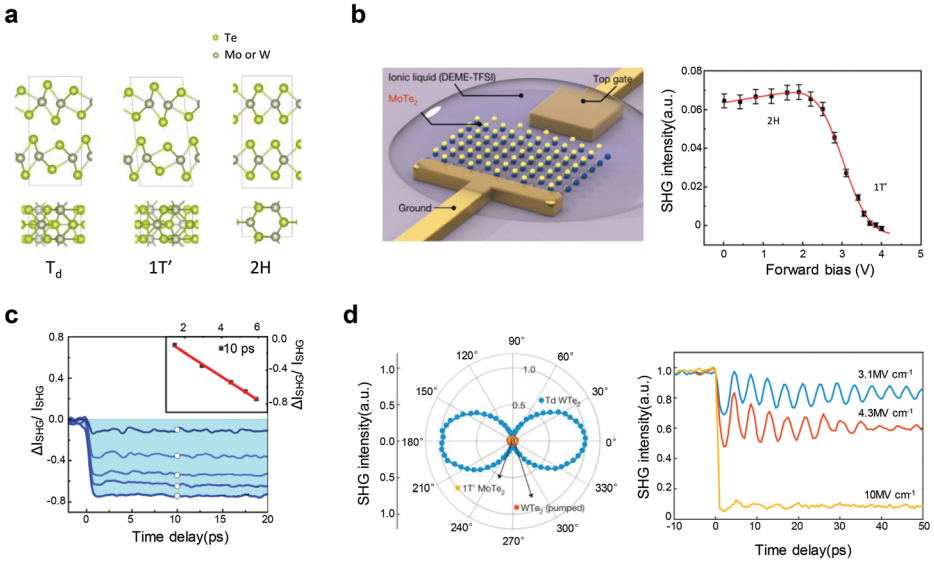

Fig. 4 Detection of phase transition and ultrafast phase transition in 2D materials by SHG. (a) Schematic of the crystal structure of the monolayer T_d-, 1T′- and 2H-phase. Reproduced from ref. 123 with permission from American Physical Society, copyright 2016. (b) Schematics configuration of a $MoTe_2$ monolayer ionic liquid field-effect transistor (left). Gate-dependent SHG intensity under forward bias (right). Reproduced from ref. 61 with permission from Springer Nature, copyright 2017. (c) Pump-induced SHG time traces of $MoTe_2$ at various pump field strengths at T = 10 K. Reproduced from ref. 68 with permission from American Physical Society, copyright 2019. (d) Polar plot of SHG intensity of angular dependence of equilibrium WTe_2 (blue), pumped WTe_2 (red) and centrosymmetric $MoTe_2$ (yellow) (left). Pump-induced SHG time traces of WTe_2 at various pump field strengths (right). Reproduced from ref. 69 with permission from Springer Nature, copyright 2019.

ment, the 2H phase monolayer $MoTe_2$ is driven to the 1T′ phase by the ionic liquid top gate (Fig. 4b).[61] 2H phase $MoTe_2$ with broken inversion symmetry generates finite SHG signal with no applied gate. When the gate further increases above 2.2 V, the SHG signal significantly decreases for more than one order of magnitude, which is a clear sign of noncentrosymmetric 2H to centrosymmetric 1T′ phase transition. The 2H to 1T′ transition can also be induced by laser irradiation, but transition in this way is sometimes irreversible. In few-layer 2H-$MoTe_2$, the polarization dependent SHG pattern changes from a six-fold pattern to a two-lobe pattern after laser ablation. The six-fold pattern represents the 2H phase of $MoTe_2$, and the two-lobe pattern is identical to the C_s^1 space group of few-layer $MoTe_2$ with even numbers.[62] It is worth noting that SHG is also a good technique to investigate ferroelectric materials.[63,64] The prerequisite for paraelectric-to-ferroelectric phase transition is symmetry breaking, which leads to the separation of the positive and negative electric charge centers and finally induces a spontaneous nonzero polarization. In this regard, SHG is a practical supplemental tool to detect ferroelectricity in the 2D limit and has already been applied in $CuInP_2S_6$, $MoTe_2$ and In_2Se_3.[65–67] 2D $CuInP_2S_6$ demonstrates room-temperature ferroelectricity with a transition temperature of about 315 K.[65] The ferroelectric phase belongs to noncentrosymmetric point group **m**, while the paraelectric phase belongs to the centrosymmetric point group **2/m**. In the temperature dependent experiment, the SHG intensity of the $CuInP_2S_6$ nanoflake gradually decreases and finally vanishes when temperature rises above transition temperature T_c. This strongly suggests a structural change from noncentrosymmetric to centrosymmetric and facilitates to capture the ferroelectric to paraelectric phase transition around T_c.

Meanwhile, as an optical technique, SHG can get access to ultrafast temporal evolution and dynamics of phase transitions in 2D materials when combined with ultrafast pump–probe and time-resolved spectroscopy. As mentioned before, $MoTe_2$ exhibits several phases and the electronic nature of these phases are different. The 1T′ phase is a normal semimetal phase, while the T_d phase is the type-II Weyl semimetal phase and is superconducting with transition temperature T_c = 0.1 K. Transition between them can be controlled in several ways. The 1T′ to T_d phase change can be realized by cooling to below 250 K. The noncentrosymmetric T_d structure in low temperature excited by ultrashort laser pulses can transform into the centrosymmetric 1T′ phase. In pump–probe SHG measurements below 250 K, the SHG intensity significantly drops to a low order around 0.7 ps after time zero, which suggests the presence of noncentrosymmetric T_d to centrosymmetric 1T′ phase transition (Fig. 4c).[68] Similarly, T_d to 1T′ phase transition in WTe_2 can be triggered by an incident terahertz light pulse.[69] The terahertz light pulse would generate large amplitude interlayer shear strain in WTe_2 which is demonstrated by ultrafast electron diffraction and then leads to the phase transition. As a supporting material to electron diffraction, it is convenient to recognize the phase transition by SHG. The polarized SHG pattern of WTe_2 in the absence of pump pulse (blue) is shown as the two-lobe pattern, which is in agreement with the T_d phase. At time delay about 2 ps, the SHG of all

polarization directions completely vanishes, just like the rapid drop of SHG intensity in the pump–probe SHG measurement, further proving the T_d to 1T′ phase transition (Fig. 4d).

As a supplement, the time dependent response of the SHG signal in Fig. 4c and d is accompanied by oscillations, that results from surface optical phonon mode. The vibration of surface phonons results in time-dependent modulation of the SHG intensity, and thus ultrafast coherent phonon spectroscopy is also an important application of time-resolved SHG.[70,71]

6. Electron–hole symmetry

Electrons and holes are basic particles for comprehension of electronic and optical properties in condensed matter physics. The symmetry between electrons with energy above the Fermi sea and holes below the Fermi energy is the fundamental property of materials such as superconductors, topological insulators and Weyl semimetals.[72–75] Graphene, the pioneer of 2D materials, possesses gapless Dirac fermions with linear dispersion and provides a good platform for studying electron–hole symmetry.[76–78] Graphene possesses a hexagonal honeycomb lattice structure and is highly symmetrical belonging to the D_{6h} point group. For such centrosymmetric materials, SHG is absent under electric dipole approximation and the first non-vanishing nonlinear process is considered to be the third order optical nonlinearity such as third harmonic generation (THG).[79–81] However, graphene still has a possibility to generate an unusual SHG response if the assumption is extended from the electric-dipole approximation to multipole approximation. Although $\chi^{(2)}_{ED}$ vanishes in monolayer graphene, higher-order multipole such as $\chi^{(3)}_{EQ}$ is still allowed. It has been theoretically proposed that the second order optical response of graphene can be generated by third order nonlinearity such as electric quadrupole-like effects. Meanwhile, the interband transitions in graphene make this nonlinear optical response rich and tunable.[82,83] Meaningfully, EQ-SHG of graphene is predicted to be sensitive to the electron–hole symmetry, which suggests SHG to be a more powerful tool in symmetry analysis.

Actually, several previous studies have detected weak SHG signal on supported graphene monolayers, whereas the SHG signal doesn't arise from intrinsic graphene but from the asymmetry interface of graphene and the substrate, which results in electric-dipole allowed SHG.[84–86] The ED- and EQ-SHG can be separately described as $P_{ED}(2\omega) = \chi^{(2)}_{ED}{:}E(\omega)E(\omega)$ and $Q(2\omega) = \chi^{(3)}_{EQ}\mathbf{q}{:}E(\omega)E(\omega)$. $\chi^{(2)}_{ED}$ is a three-rank tensor mainly correlating to the spatial symmetry of the medium, while $\chi^{(3)}_{EQ}$ is a four-rank susceptibility tensor and $\mathbf{q}$ is the photon wave vector. Usually, a common normal incidence experiment does not involve the z components of the susceptibility tensor, in contrast, an oblique incidence experiment, as shown in Fig. 5a, does involve different linear combinations of the tensor elements. Therefore, different distributions of nonzero tensor elements for EQ-SHG and ED-SHG lead to their opposite performance under different excitation geometries. The intensity ratio between the normal and 45° oblique incidence of EQ- and ED-SHG is calculated as 0% and 96% respectively. The giant difference facilitates exclusion of interface ED-SHG from EQ-SHG. The ratio was experimentally confirmed to be 0.6%, which guarantees that EQ-SHG is the dominant signal in the oblique incident experiment of monolayer graphene.[27]

The inversion of the electron band and hole band of graphene is depicted in Fig. 5b under the operation of electron–hole symmetry for $\mu \rightarrow -\mu$ ($\mathbf{k} \rightarrow -\mathbf{k}$) and time-reversal symmetry for $\mathbf{q} \rightarrow -\mathbf{q}$, where μ is the chemical potential, and $\mathbf{q}$ and $\mathbf{k}$ are the photon wave vector and electron wave vector. The elements in $\chi^{(3)}_{EQ}(\mu,\mathbf{q})$ at $\mathbf{q}$ and μ evolve as $\chi^{(3)}_{EQ}(\mu,\mathbf{q}) = \chi^{(3)}_{EQ}(-\mu,-\mathbf{q}) = -\chi^{(3)}_{EQ}(-\mu,\mathbf{q})$. The sign of $\chi^{(3)}_{EQ}$ changes when inverting electron and hole bands, which means an odd parity with respect to μ. Accordingly, the EQ-SHG response in graphene is sensitive to chemical potential or carrier doping and strictly vanishes at the charge neutral point. In the ion-gel gating experiment, the excitation beam with a photon energy of 0.95 eV incident at 45° from the surface normal of monolayer graphene and the chemical potential μ of graphene could be tuned from −0.9 to 0.5 eV. Prominently, no apparent EQ-SHG signal can be detected at the charge neutral point of chemical potential μ, but it significantly increases with an increase in $|\mu|$. The μ dependence of oblique EQ-SHG also reveals the resonant transitions in the linearly dispersed band structure of graphene. Fig. 5c shows the oblique SHG variation with respect to μ for s- and p-polarized excitation. Two little peaks of $|\chi^{(3)}_{EQ}q_x|$ are sep-

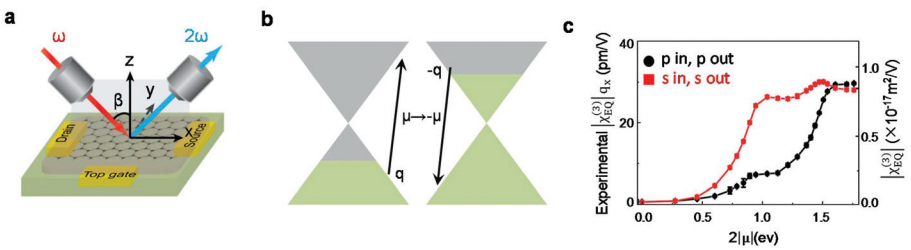

Fig. 5 Detection of electron–hole symmetry in graphene. (a) Schematic of experimental geometry about the SHG process of ion-gel gated graphene at an oblique incidence of 45°. (b) Transition schematics under electron–hole symmetry and time-reversal symmetry operation, where **k** and **q** electron wave vector and the photon wave vector. (c) Experimentally extracted second-order nonlinear susceptibility $|\chi^{(3)}_{EQ}q_x|$ of SHG for s- and p-polarized excitations. Reproduced from ref. 27 with permission from American Physical Society, copyright 2019.

arately around the one-photon ($2|\mu| = \hbar\omega$) and two-photon ($|\mu| = \hbar\omega$) energy resonance of the incident light.

7. Antiferromagnetic order

Antiferromagnetism is a type of magnetism where the magnetic moments of neighboring atoms are anti-parallel. It is considered to have promising potential for spintronics and memory devices due to fast spin dynamics and no stray magnetic fields.[87,88] The magnetic orders of 2D layered AF materials can be basically divided into two types, that is, the type of interlayer AF order with intralayer ferromagnetic (FM) order, such as bilayer CrI_3; and the other types with intralayer AF order, mainly including the rich family of transition metal thiophosphates MPS_3 (M = Mn, Fe, Co or Ni) and selenophosphates $MPSe_3$ (M = Mn, Fe or Ni).[19]

In contrast to a ferromagnet, an antiferromagnet in spite of hosting an ordered state does not exhibit any net magnetization, which means it is unable to be detected by the magneto optical Kerr rotation experiment. Neutron diffraction can reveal the hidden AF order of bulk materials, whereas it fails to show its magical power when dealing with atomically thin layers. Since the AF order can be understood from the perspective of corresponding symmetry breaking, it is possible to detect AF order through the SHG technique.[87] In particular, several AF orders break both the spatial-inversion symmetry and time-reversal symmetry, thus inducing strong time-noninvariant electric-dipole-allowed SHG, namely, c-type ED-SHG whether the medium is centrosymmetric or not. The c-type ED-SHG has already been used to probe antiferromagnetic order in many bulk crystals such as Cr_2O_3.[13]

Bulk CrI_3 is a ferromagnet below the Curie temperature $T_c \approx 60$ K and monolayer CrI_3 is also a ferromagnet with a centrosymmetric lattice structure.[89] In contrast, bilayer CrI_3 remains centrosymmetric but possessing interlayer AF order with a Néel temperature $T_{AF} \approx 45$ K.[90] Uncovering the stacking structure and magnetic structure of bilayer CrI_3 is very important for understanding its layer dependent magnetism. Fig. 6a shows two magnetic order states of bilayer CrI_3. When the bilayer CrI_3 is interlayer antiferromagnetically aligned, it is structurally reversed under spatial-inversion ($r \rightarrow -r$) operation or time-reversal ($t \rightarrow -t$) operation. In contrast, it remains unchanged after spatial-inversion operation if it is in the interlayer ferromagnetically aligned state. Thus, the AF state can generate c-type ED-SHG, while the FM state cannot.[91] Above the critical temperature, SHG from the lattice structure is forbidden and no magnetic order generates SHG signal, so no SHG signal is detected. When bilayer CrI_3 is cooled below the critical temperature, although the centrosymmetric lattice structure still gives no contribution, the emerging AF order provides measurable SHG-signal. A significant difference between above and below the critical temperature is experimentally in agreement with that (Fig. 6a).

It has been theoretically proved that bulk CrI_3 goes through a structural phase transition changing from a high temperature monoclinic stacking which tends to form AF coupling to a low temperature rhombohedral stacking which is inclined to behave FM at around 200 K.[92,93] According to symmetry analysis, the rhombohedral structure belongs to the S_6 crystallo-

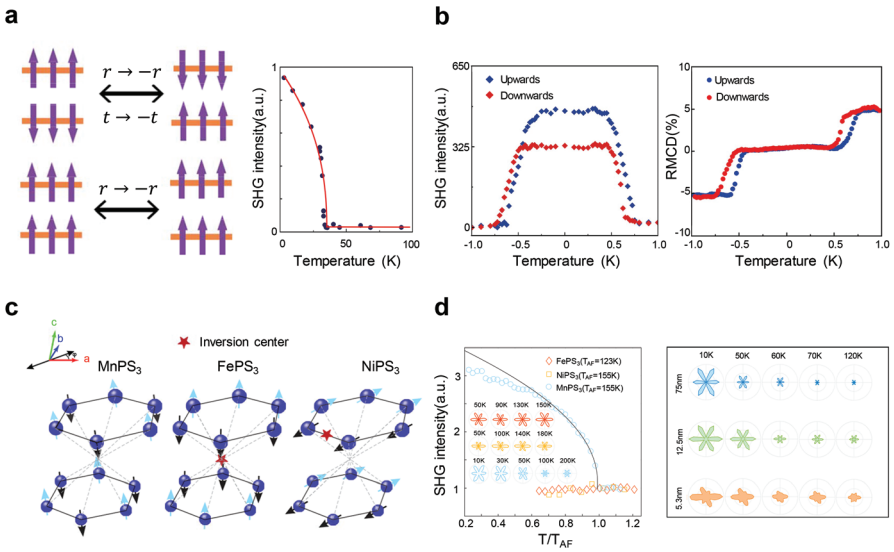

Fig. 6 Antiferromagnetic order characterization by SHG. (a) Schematics of symmetry operation of antiferromagnetic and ferromagnetic states of bilayer CrI_3 (left). Temperature dependent SHG intensity of the bilayer CrI_3 (right). (b) Magnetic field dependent circularly polarized SHG intensity (left) and RMCD hysteresis loop (right). (a, b) Reproduced from ref. 91 with permission from Springer Nature, copyright 2019. (c) Schematics of AF structures of $MnPS_3$, $FePS_3$ and $NiPS_3$. Arrows and stars indicate the spin orientation and inversion center of the AF structure, respectively. (d) Temperature dependence of the polarization resolved SHG patterns of $MnPS_3$, $FePS_3$ and $NiPS_3$ (left). Temperature dependent polarization resolved SHG patterns from $MnPS_3$ flakes of thicknesses of 75 nm, 12.5 nm and 5.3 nm (right). (c, d) Reproduced from ref. 97 with permission from American Physical Society, copyright 2020.

graphic point group, which lacks a mirror plane. In contrast, the monoclinic structure possesses C_{2h} symmetry, which has a mirror plane. The polarization resolved SHG pattern of bilayer CrI_3 is always accompanied by a mirror plane, which is in accordance with the monoclinic stacking structure, confirming that the monoclinic phase still persists in bilayer CrI_3. Reflectance magneto-circular dichroism (RMCD) is commonly used to probe 2D magnetic materials, which is zero in the layered antiferromagnetic state and non-zero when spin ferromagnetically aligned. For bilayer CrI_3, magnetic field dependent circularly polarized SHG combined with RMCD clearly depicts a complete picture of the switch between different magnetic states (Fig. 6b).

The intralayer AF orders can be further divided into AF-Néel ($MnPS_3$), AF-zigzag ($FePS_3$ and $NiPS_3$) and AF-stripy states. Bulk $MnPS_3$ with AF-Néel order is widely studied for the linear magnetoelectric (ME) effect which holds great potential for electric field control of magnetism for spintronics and applications in memory devices and sensors.[94–96] $MnPS_3$, $FePS_3$ and $NiPS_3$ exhibit similar centrosymmetric lattice structures. Conversely, AF order in bulk $MnPS_3$ breaks inversion symmetry while in bulk $FePS_3$ and $NiPS_3$ hosts inversion symmetry (Fig. 6c). As a result, AF order in bulk $MnPS_3$ will contribute c-type ED-SHG but in $FePS_3$ and $NiPS_3$ will not.[97] All three bulk crystals generate finite SHG signal above critical temperature T_{AF} which are contributed to bulk EQ-SHG. Below T_{AF}, $FePS_3$ and $NiPS_3$ have no apparent change. In contrast, SHG of $MnPS_3$ achieves a rapid increase, which is consistent with the hypothesis that EQ-SHG gives fixed contribution and the emerging non-centrosymmetric AF order leads to c-type ED-SHG below T_{AF}. When continually reducing the thickness of $MnPS_3$ down to few layer thickness, temperature dependent SHG rotational anisotropy patterns of different thicknesses behave similarly to bulk $MnPS_3$, which is solid evidence that the Néel order in bulk $MnPS_3$ is preserved and even exfoliated down to the ultrathin limit (Fig. 6d).

8. Large enhancement and tunability of SHG

2D materials exhibit unexpectedly high nonlinear optical susceptibility, which is even larger than many conventional nonlinear bulk crystals. However, the atomic scale thickness greatly limits nonlinear light–matter interaction length and results in relatively low frequency conversion efficiency. To address this issue, two available strategies are mainly used to improve the conversion efficiency: (1) exciton resonance enhancement and (2) integrating 2D materials with nanophotonics.

Owing to the large binding energy, optical responses of 2D materials are dominated by excitonic effects. The strongly bound excitons provide a new approach to enhance light–matter interactions and exhibit large tunability on 2D material nonlinearity at the atomic thickness scale. It is demonstrated that SHG intensity of monolayer WSe_2 under excitation in resonance with the exciton state is enhanced by up to 3 orders of magnitude with respect to off resonance.[36] Based on this, electrically controlled SHG is achieved in monolayer WSe_2 field-effect transistors due to different excitonic resonance states at different electrical doping levels.[37] Recently, gate-tunable four-wave mixing and sum-frequency generation are investigated in ion-gel-gated monolayer MoS_2 devices, which further proves that excitonic effects have a giant impact on the modulation of nonlinear optical properties of 2D materials and provides a promising path for electrically tunable nonlinear optical devices.[98]

On the other hand, hybrid systems of 2D materials and silicon photonics open a new path for nonlinearity enhancement. One typical way is to combine 2D materials with optical cavity. Photonic crystal (PC) cavities with small mode volume and high Q can effectively enhance the nonlinear optical interaction in 2D materials. Local optical field is significantly enhanced as light is confined in a small volume. In addition,

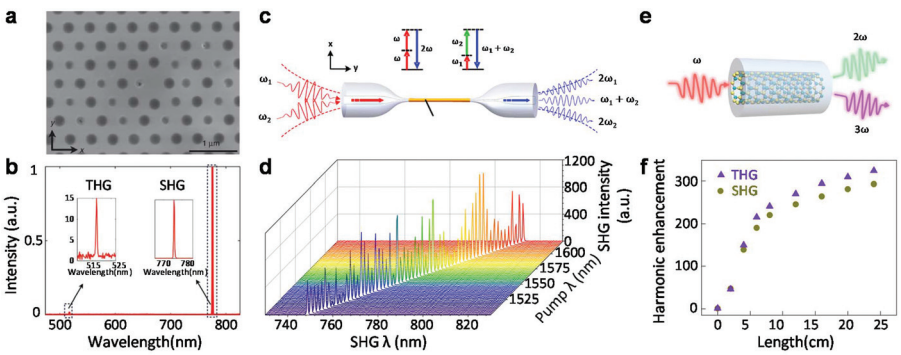

Fig. 7 Large enhancement and tunability of SHG in 2D materials. (a) SEM image of the GaSe-PC cavity. (b) SHG and THG spectra of GaSe-PC cavity pumped by continuous-wave 1551 nm laser. (a, b) Reproduced from ref. 101 with permission from Springer Nature, copyright 2018.(c) Schematic of SHG and SFG process from the GaSe-integrated microfibre. (d) SHG spectra with different pump wavelengths changing from 1500 nm to 1620 nm. (c, d) Reproduced from ref. 102 with permission from Springer Nature, copyright 2020. (e) Schematics of SHG and THG processes in MoS_2-embedded HCF. (f) Fibre-length-dependent SHG and THG enhancements in MoS_2. (e, f) Reproduced from ref. 104 with permission from Springer Nature, copyright 2020.

PC-cavities can store light for an extended period of time and therefore increase the light–matter interaction time. SHG intensity of monolayer WSe_2 is enhanced by a factor of ~200 after integrating on silicon PC-cavities under 1550 nm laser excitation which is near the resonance modes of the cavity.[99] Monolayer MoS_2 embedded within an all-dielectric Fabry–Pérot microcavity claims over one order of magnitude in spite of its relatively low-Q.[100] The remarkable enhancement of SHG significantly reduces the threshold of excitation power. In general, pulsed lasers are employed to realize SHG signal due to high peak pump power. With the aid of cavity enhancement, continuous-wave pumped SHG is achieved in few- and monolayer GaSe flake coated PC-cavities (Fig. 7a).[101] In a nine-layer GaSe coated PC cavity, comparing SHG originating from GaSe and THG arising from silicon slab, the SHG peak is stronger than the THG peak over 650 times (Fig. 7b). Another applicable way is to combine 2D materials with optical fibres. The long and controllable interaction length of optical fibres and the high power density of fibre cores permit ultrahigh efficiency SHG conversions. In GaSe-deposited microfibres, strong SHG signals can be obtained with only sub-milliwatt continuous-wave lasers in a wide wavelength range (1500–1620 nm) which covers the whole C and L telecom bands (Fig. 7c and d).[102] Recent progress in 2D material growth makes it realistic to directly grow 2D materials in optical fibres.[103,104] In a 25 cm-long fibre MoS_2-embedded hollow capillary fibre, both SHG and THG can be enhanced by 300 times in contrast to monolayer MoS_2/silica (Fig. 7e and f).[104] Besides optical cavities and fibres, there still remain many promising approaches which can provide localized enhancement and be able to modulate the optical nonlinearities in 2D materials such as plasmonics, waveguide integration and optical resonators, which provides the possibility to expand the applications of 2D materials in nonlinear optical chip-integrated devices.[105,106]

9. Summary and outlook

In summary, SHG is a powerful, versatile and simple technique to unveil the physical properties of 2D materials. Based on its extreme sensitivity to spatial-inversion symmetry and time-reversal symmetry, we review five aspects of SHG applied in 2D materials, *i.e.* crystal structure characterization, strain visualization, phase transition, electron–hole symmetry and antiferromagnetic order detection in 2D materials, extending from the electric-dipole approximation to multipole approximation.

Despite the rapid progress of SHG applied in 2D materials, there is still a lot of room for its growth and development. $\chi^{(2)}$ can extensively be regarded as a function of order parameters.[107] Besides probing magnetic order, the extreme sensitivity to both spatial-inversion symmetry and time-reversal symmetry permits SHG to unveil many other complicated orders such as ferro-rotational order in $RbFe(MoO_4)_2$ and ferrotoroidic order in $LiCoPO_4$.[108,109] In many complex oxides, such order always relates to crystallographic fine structural distortion of oxygen atoms.[110] The small distortion sometimes even cannot be revealed by TEM since it may fail to format effective contrast between heavy elements and oxygen.[111] SHG spectroscopy could be an alternative to detect order parameters and the related fine structure distortion in 2D complex oxides. Since SHG can be combined with the pump–probe technique, it also provides the possibility to probe ultrafast order parameter dynamics under external excitation. In addition, since multiphoton processes exhibit different optical selection rules compared with linear optical response, SHG provides a new platform to explore intriguing physics such as dark excitons and valley degree of freedom.[36,112–115] Combined with strong exciton effects, SHG can facilitate the exploration of exotic exciton states such as recently reported excited states of exciton polaritons in WS_2.[116]

Additionally, it has already been proved that some inversion broken Weyl semimetals and topological insulators, such as TaAs and Bi_2Se_3, can generate considerable SHG signals.[117–119] Sensitivity to the charge neutral point of SHG in graphene also gives a new perspective to utilize such response to study related Dirac materials. So, benefitting from all the listed advantages of SHG, we believe that the nonlinear SHG approach will shed light on more novel properties of 2D materials in the future and promote the development of the constantly growing 2D material family.

Conflicts of interest

There are no conflicts to declare.

Acknowledgements

This work was supported by the Beijing Natural Science Foundation (JQ19004), the National Natural Science Foundation of China (52025023, 51991340, and 51991342), the National Key R&D Program of China (2016YFA0300903 and 2016YFA0300804), the Beijing Excellent Talents Training Support – Top Young Individual Project (2017000026833ZK11), the Key R&D Program of Guangdong Province (2020B010189001, 2019B010931001, and 2018B030327001), the Beijing Municipal Science & Technology Commission (Z191100007219005), the Beijing Graphene Innovation Program (Z181100004818003), the National Equipment Program of China (ZDYZ2015-1), the Bureau of Industry and Information Technology of Shenzhen (No. 201901161512).

References

1 P. A. Franken, A. E. Hill, C. W. Peters and G. Weinreich, *Phys. Rev. Lett.*, 1961, **7**, 118–119.
2 R. M. Corn and D. A. Higgins, *Chem. Rev.*, 1994, **94**, 107–125.
3 M. Fiebig, V. V. Pavlov and R. V. Pisarev, *J. Opt. Soc. Am. B*, 2005, **22**, 96–118.

4 P. Pantazis, J. Maloney, D. Wu and S. E. Fraser, *Proc. Natl. Acad. Sci. U. S. A.*, 2010, **107**, 14535–14540.
5 R. V. Pisarev, B. Kaminski, M. Lafrentz, V. V. Pavlov, D. R. Yakovlev and M. Bayer, *Phys. Status Solidi B*, 2010, **247**, 1498–1504.
6 G. Berkovic, G. Marowsky, R. Steinhoff and Y. R. Shen, *J. Opt. Soc. Am. B*, 1989, **6**, 205–208.
7 Y. R. Shen, *Nature*, 1989, **337**, 519–525.
8 N. Kato, *Biophys. Rev.*, 2019, **11**, 399–408.
9 E. W. Meijer, E. E. Havinga and G. L. Rikken, *Phys. Rev. Lett.*, 1990, **65**, 37–39.
10 S. Qin, W. M. You and Z. B. Su, *Phys. Rev. B: Condens. Matter Mater. Phys.*, 1993, **48**, 17562–17568.
11 B. Koopmans, A. M. Janner, H. T. Jonkman, G. A. Sawatzky and F. van der Woude, *Phys. Rev. Lett.*, 1993, **71**, 3569–3572.
12 M. Fiebig, D. Frohlich, K. Kohn, S. Leute, T. Lottermoser, V. V. Pavlov and R. V. Pisarev, *Phys. Rev. Lett.*, 2000, **84**, 5620–5623.
13 M. Fiebig, D. Frohlich, B. B. Krichevtsov and R. V. Pisarev, *Phys. Rev. Lett.*, 1994, **73**, 2127–2130.
14 J. Hohlfeld, E. Matthias, R. Knorren and K. H. Bennemann, *Phys. Rev. Lett.*, 1997, **78**, 4861–4864.
15 T. F. Nova, A. S. Disa, M. Fechner and A. Cavalleri, *Science*, 2019, **364**, 1075–1079.
16 C. Tzschaschel, T. Satoh and M. Fiebig, *Nat. Commun.*, 2019, **10**, 3995.
17 K. S. Novoselov, A. K. Geim, S. V. Morozov, D. Jiang, Y. Zhang, S. V. Dubonos, I. V. Grigorieva and A. A. Firsov, *Science*, 2004, **306**, 666–669.
18 G. B. Liu, D. Xiao, Y. Yao, X. Xu and W. Yao, *Chem. Soc. Rev.*, 2015, **44**, 2643–2663.
19 K. F. Mak, J. Shan and D. C. Ralph, *Nat. Rev. Phys.*, 2019, **1**, 646–661.
20 A. H. Castro Neto, F. Guinea, N. M. R. Peres, K. S. Novoselov and A. K. Geim, *Rev. Mod. Phys.*, 2009, **81**, 109–162.
21 L. Britnell, R. M. Ribeiro, A. Eckmann, R. Jalil, B. D. Belle, A. Mishchenko, Y. J. Kim, R. V. Gorbachev, T. Georgiou, S. V. Morozov, A. N. Grigorenko, A. K. Geim, C. Casiraghi, A. H. Castro Neto and K. S. Novoselov, *Science*, 2013, **340**, 1311–1314.
22 F. Xia, H. Wang, D. Xiao, M. Dubey and A. Ramasubramaniam, *Nat. Photonics*, 2014, **8**, 899–907.
23 D. Hu, X. Yang, C. Li, R. Liu, Z. Yao, H. Hu, S. N. G. Corder, J. Chen, Z. Sun, M. Liu and Q. Dai, *Nat. Commun.*, 2017, **8**, 1471.
24 M. Chubarov, T. H. Choudhury, X. Zhang and J. M. Redwing, *Nanotechnology*, 2018, **29**, 055706.
25 L. Wang, X. Xu, L. Zhang, R. Qiao, M. Wu, Z. Wang, S. Zhang, J. Liang, Z. Zhang, Z. Zhang, W. Chen, X. Xie, J. Zong, Y. Shan, Y. Guo, M. Willinger, H. Wu, Q. Li, W. Wang, P. Gao, S. Wu, Y. Zhang, Y. Jiang, D. Yu, E. Wang, X. Bai, Z. J. Wang, F. Ding and K. Liu, *Nature*, 2019, **570**, 91–95.
26 A. Saynatjoki, L. Karvonen, H. Rostami, A. Autere, S. Mehravar, A. Lombardo, R. A. Norwood, T. Hasan, N. Peyghambarian, H. Lipsanen, K. Kieu, A. C. Ferrari, M. Polini and Z. Sun, *Nat. Commun.*, 2017, **8**, 893.
27 Y. Zhang, D. Huang, Y. Shan, T. Jiang, Z. Zhang, K. Liu, L. Shi, J. Cheng, J. E. Sipe, W. T. Liu and S. Wu, *Phys. Rev. Lett.*, 2019, **122**, 047401.
28 Y. L. Li, Y. Rao, K. F. Mak, Y. M. You, S. Y. Wang, C. R. Dean and T. F. Heinz, *Nano Lett.*, 2013, **13**, 3329–3333.
29 N. Kumar, S. Najmaei, Q. Cui, F. Ceballos, P. M. Ajayan, J. Lou and H. Zhao, *Phys. Rev. B: Condens. Matter Mater. Phys.*, 2013, **87**, 161403.
30 A. Autere, H. Jussila, A. Marini, J. R. M. Saavedra, Y. Dai, A. Säynätjoki, L. Karvonen, H. Yang, B. Amirsolaimani, R. A. Norwood, N. Peyghambarian, H. Lipsanen, K. Kieu, F. J. G. de Abajo and Z. Sun, *Phys. Rev. B*, 2018, **98**, 115426.
31 L. Karvonen, A. Saynatjoki, M. J. Huttunen, A. Autere, B. Amirsolaimani, S. Li, R. A. Norwood, N. Peyghambarian, H. Lipsanen, G. Eda, K. Kieu and Z. Sun, *Nat. Commun.*, 2017, **8**, 15714.
32 A. Autere, H. Jussila, Y. Dai, Y. Wang, H. Lipsanen and Z. Sun, *Adv. Mater.*, 2018, **30**, e1705963.
33 J. Cheng, T. Jiang, Q. Ji, Y. Zhang, Z. Li, Y. Shan, Y. Zhang, X. Gong, W. Liu and S. Wu, *Adv. Mater.*, 2015, **27**, 4069–4074.
34 X. Yin, Z. Ye, D. A. Chenet, Y. Ye, K. O'Brien, J. C. Hone and X. Zhang, *Science*, 2014, **344**, 488–490.
35 M. L. Trolle, Y.-C. Tsao, K. Pedersen and T. G. Pedersen, *Phys. Rev. B: Condens. Matter Mater. Phys.*, 2015, **92**, 161409.
36 G. Wang, X. Marie, I. Gerber, T. Amand, D. Lagarde, L. Bouet, M. Vidal, A. Balocchi and B. Urbaszek, *Phys. Rev. Lett.*, 2015, **114**, 097403.
37 K. L. Seyler, J. R. Schaibley, P. Gong, P. Rivera, A. M. Jones, S. Wu, J. Yan, D. G. Mandrus, W. Yao and X. Xu, *Nat. Nanotechnol.*, 2015, **10**, 407–411.
38 A. K. Geim and I. V. Grigorieva, *Nature*, 2013, **499**, 419–425.
39 F. Zhang, B. Sahu, H. Min and A. H. MacDonald, *Phys. Rev. B: Condens. Matter Mater. Phys.*, 2010, **82**, 035409.
40 C. H. Lui, Z. Li, K. F. Mak, E. Cappelluti and T. F. Heinz, *Nat. Phys.*, 2011, **7**, 944–947.
41 S. H. Jhang, M. F. Craciun, S. Schmidmeier, S. Tokumitsu, S. Russo, M. Yamamoto, Y. Skourski, J. Wosnitza, S. Tarucha, J. Eroms and C. Strunk, *Phys. Rev. B: Condens. Matter Mater. Phys.*, 2011, **84**, 161408.
42 C. H. Lui, Z. Li, Z. Chen, P. V. Klimov, L. E. Brus and T. F. Heinz, *Nano Lett.*, 2011, **11**, 164–169.
43 K. Liu, L. Zhang, T. Cao, C. Jin, D. Qiu, Q. Zhou, A. Zettl, P. Yang, S. G. Louie and F. Wang, *Nat. Commun.*, 2014, **5**, 4966.
44 M. Liao, Z. Wei, L. Du, Q. Wang, J. Tang, H. Yu, F. Wu, J. Zhao, X. Xu, B. Han, K. Liu, P. Gao, T. Polcar, Z. Sun, D. Shi, R. Yang and G. Zhang, *Nat. Commun.*, 2020, **11**, 2153.

45 Y. Shan, Y. Li, D. Huang, Q. Tong, W. Yao, W. T. Liu and S. Wu, *Sci. Adv.*, 2018, **4**, eaat0074.
46 W. T. Hsu, Z. A. Zhao, L. J. Li, C. H. Chen, M. H. Chiu, P. S. Chang, Y. C. Chou and W. H. Chang, *ACS Nano*, 2014, **8**, 2951–2958.
47 K. Liu and J. Q. Wu, *J. Mater. Res.*, 2016, **31**, 832–844.
48 D. Akinwande, C. J. Brennan, J. S. Bunch, P. Egberts, J. R. Felts, H. J. Gao, R. Huang, J. S. Kim, T. Li, Y. Li, K. M. Liechti, N. S. Lu, H. S. Park, E. J. Reed, P. Wang, B. I. Yakobson, T. Zhang, Y. W. Zhang, Y. Zhou and Y. Zhu, *Extreme Mech. Lett.*, 2017, **13**, 42–77.
49 X. Li, M. Sun, C. X. Shan, Q. Chen and X. L. Wei, *Adv. Mater. Interfaces*, 2018, **5**, 1701246.
50 J. H. Kim, J. H. Jeong, N. Kim, R. Joshi and G. H. Lee, *J. Phys. D: Appl. Phys.*, 2019, **52**, 083001.
51 H. Yoo, R. Engelke, S. Carr, S. Fang, K. Zhang, P. Cazeaux, S. H. Sung, R. Hovden, A. W. Tsen, T. Taniguchi, K. Watanabe, G. C. Yi, M. Kim, M. Luskin, E. B. Tadmor, E. Kaxiras and P. Kim, *Nat. Mater.*, 2019, **18**, 448–453.
52 J. Liang, J. Zhang, Z. Li, H. Hong, J. Wang, Z. Zhang, X. Zhou, R. Qiao, J. Xu, P. Gao, Z. Liu, Z. Liu, Z. Sun, S. Meng, K. Liu and D. Yu, *Nano Lett.*, 2017, **17**, 7539–7543.
53 L. Mennel, M. M. Furchi, S. Wachter, M. Paur, D. K. Polyushkin and T. Mueller, *Nat. Commun.*, 2018, **9**, 516.
54 X. X. Xi, Z. F. Wang, W. W. Zhao, J. H. Park, K. T. Law, H. Berger, L. Forro, J. Shan and K. F. Mak, *Nat. Phys.*, 2016, **12**, 139–143.
55 E. Navarro-Moratalla, J. O. Island, S. Manas-Valero, E. Pinilla-Cienfuegos, A. Castellanos-Gomez, J. Quereda, G. Rubio-Bollinger, L. Chirolli, J. A. Silva-Guillen, N. Agrait, G. A. Steele, F. Guinea, H. S. van der Zant and E. Coronado, *Nat. Commun.*, 2016, **7**, 11043.
56 C. Gong, L. Li, Z. Li, H. Ji, A. Stern, Y. Xia, T. Cao, W. Bao, C. Wang, Y. Wang, Z. Q. Qiu, R. J. Cava, S. G. Louie, J. Xia and X. Zhang, *Nature*, 2017, **546**, 265–269.
57 W. G. Dawson and D. W. Bullett, *J. Phys. C: Solid State Phys.*, 1987, **20**, 6159–6174.
58 R. Clarke, E. Marseglia and H. P. Hughes, *Philos. Mag. B*, 2006, **38**, 121–126.
59 Y. Sun, S.-C. Wu, M. N. Ali, C. Felser and B. Yan, *Phys. Rev. B: Condens. Matter Mater. Phys.*, 2015, **92**, 161107.
60 H.-J. Kim, S.-H. Kang, I. Hamada and Y.-W. Son, *Phys. Rev. B*, 2017, **95**, 180101.
61 Y. Wang, J. Xiao, H. Zhu, Y. Li, Y. Alsaid, K. Y. Fong, Y. Zhou, S. Wang, W. Shi, Y. Wang, A. Zettl, E. J. Reed and X. Zhang, *Nature*, 2017, **550**, 487–491.
62 Y. Song, R. Tian, J. Yang, R. Yin, J. Zhao and X. Gan, *Adv. Opt. Mater.*, 2018, **6**, 1701334.
63 S. A. Denev, T. T. A. Lummen, E. Barnes, A. Kumar, V. Gopalan and D. J. Green, *J. Am. Ceram. Soc.*, 2011, **94**, 2699–2727.
64 Z. Guan, H. Hu, X. Shen, P. Xiang, N. Zhong, J. Chu and C. Duan, *Adv. Electron. Mater.*, 2019, **6**, 1900818.
65 F. Liu, L. You, K. L. Seyler, X. Li, P. Yu, J. Lin, X. Wang, J. Zhou, H. Wang, H. He, S. T. Pantelides, W. Zhou, P. Sharma, X. Xu, P. M. Ajayan, J. Wang and Z. Liu, *Nat. Commun.*, 2016, **7**, 12357.
66 J. Xiao, H. Zhu, Y. Wang, W. Feng, Y. Hu, A. Dasgupta, Y. Han, Y. Wang, D. A. Muller, L. W. Martin, P. Hu and X. Zhang, *Phys. Rev. Lett.*, 2018, **120**, 227601.
67 S. Yuan, X. Luo, H. L. Chan, C. Xiao, Y. Dai, M. Xie and J. Hao, *Nat. Commun.*, 2019, **10**, 1775.
68 M. Y. Zhang, Z. X. Wang, Y. N. Li, L. Y. Shi, D. Wu, T. Lin, S. J. Zhang, Y. Q. Liu, Q. M. Liu, J. Wang, T. Dong and N. L. Wang, *Phys. Rev. X*, 2019, **9**, 021036.
69 E. J. Sie, C. M. Nyby, C. D. Pemmaraju, S. J. Park, X. Shen, J. Yang, M. C. Hoffmann, B. K. Ofori-Okai, R. Li, A. H. Reid, S. Weathersby, E. Mannebach, N. Finney, D. Rhodes, D. Chenet, A. Antony, L. Balicas, J. Hone, T. P. Devereaux, T. F. Heinz, X. Wang and A. M. Lindenberg, *Nature*, 2019, **565**, 61–66.
70 W. A. Tisdale, K. J. Williams, B. A. Timp, D. J. Norris, E. S. Aydil and X. Y. Zhu, *Science*, 2010, **328**, 1543–1547.
71 L. Du, J. Tang, Y. Zhao, X. Li, R. Yang, X. Hu, X. Bai, X. Wang, K. Watanabe, T. Taniguchi, D. Shi, G. Yu, X. Bai, T. Hasan, G. Zhang and Z. Sun, *Adv. Funct. Mater.*, 2019, **29**, 1904734.
72 S. Ryu and Y. Hatsugai, *Phys. Rev. Lett.*, 2002, **89**, 077002.
73 P. Jarillo-Herrero, S. Sapmaz, C. Dekker, L. P. Kouwenhoven and H. S. Van Der Zant, *Nature*, 2004, **429**, 389–392.
74 Z. P. Yin, S. Lebegue, M. J. Han, B. P. Neal, S. Y. Savrasov and W. E. Pickett, *Phys. Rev. Lett.*, 2008, **101**, 047001.
75 A. R. Wright and R. H. McKenzie, *Phys. Rev. B: Condens. Matter Mater. Phys.*, 2013, **87**, 085411.
76 V. M. Pereira, F. Guinea, J. M. Lopes dos Santos, N. M. Peres and A. H. Castro Neto, *Phys. Rev. Lett.*, 2006, **96**, 036801.
77 J. Yan, Y. Zhang, P. Kim and A. Pinczuk, *Phys. Rev. Lett.*, 2007, **98**, 166802.
78 J. Li, L. Lin, D. Rui, Q. Li, J. Zhang, N. Kang, Y. Zhang, H. Peng, Z. Liu and H. Q. Xu, *ACS Nano*, 2017, **11**, 4641–4650.
79 S.-Y. Hong, J. I. Dadap, N. Petrone, P.-C. Yeh, J. Hone and R. M. Osgood, *Phys. Rev. X*, 2013, **3**, 085411.
80 N. Kumar, J. Kumar, C. Gerstenkorn, R. Wang, H.-Y. Chiu, A. L. Smirl and H. Zhao, *Phys. Rev. B: Condens. Matter Mater. Phys.*, 2013, **87**, 121406.
81 T. Jiang, D. Huang, J. Cheng, X. Fan, Z. Zhang, Y. Shan, Y. Yi, Y. Dai, L. Shi, K. Liu, C. Zeng, J. Zi, J. E. Sipe, Y.-R. Shen, W.-T. Liu and S. Wu, *Nat. Photonics*, 2018, **12**, 430–436.
82 Y. Wang, M. Tokman and A. Belyanin, *Phys. Rev. B*, 2016, **94**, 195442.
83 J. L. Cheng, N. Vermeulen and J. E. Sipe, *Sci. Rep.*, 2017, **7**, 43843.
84 J. J. Dean and H. M. van Driel, *Appl. Phys. Lett.*, 2009, **95**, 261910.

85 A. Y. Bykov, T. V. Murzina, M. G. Rybin and E. D. Obraztsova, *Phys. Rev. B: Condens. Matter Mater. Phys.*, 2012, **85**, 121413.
86 S. Mubeen, N. Singh, J. Lee, G. D. Stucky, M. Moskovits and E. W. McFarland, *Nano Lett.*, 2013, **13**, 2110–2115.
87 P. Němec, M. Fiebig, T. Kampfrath and A. V. Kimel, *Nat. Phys.*, 2018, **14**, 229–241.
88 J. Železný, P. Wadley, K. Olejník, A. Hoffmann and H. Ohno, *Nat. Phys.*, 2018, **14**, 220–228.
89 B. Huang, G. Clark, E. Navarro-Moratalla, D. R. Klein, R. Cheng, K. L. Seyler, D. Zhong, E. Schmidgall, M. A. McGuire, D. H. Cobden, W. Yao, D. Xiao, P. Jarillo-Herrero and X. Xu, *Nature*, 2017, **546**, 270–273.
90 B. Huang, G. Clark, D. R. Klein, D. MacNeill, E. Navarro-Moratalla, K. L. Seyler, N. Wilson, M. A. McGuire, D. H. Cobden, D. Xiao, W. Yao, P. Jarillo-Herrero and X. Xu, *Nat. Nanotechnol.*, 2018, **13**, 544–548.
91 Z. Sun, Y. Yi, T. Song, G. Clark, B. Huang, Y. Shan, S. Wu, D. Huang, C. Gao, Z. Chen, M. McGuire, T. Cao, D. Xiao, W. T. Liu, W. Yao, X. Xu and S. Wu, *Nature*, 2019, **572**, 497–501.
92 M. A. McGuire, H. Dixit, V. R. Cooper and B. C. Sales, *Chem. Mater.*, 2015, **27**, 612–620.
93 P. Jiang, C. Wang, D. Chen, Z. Zhong, Z. Yuan, Z.-Y. Lu and W. Ji, *Phys. Rev. B*, 2019, **99**, 144401.
94 M. Fiebig, *J. Phys. D: Appl. Phys.*, 2005, **38**, R123–R152.
95 J. P. Rivera, *Eur. Phys. J. B*, 2009, **71**, 299–313.
96 E. Ressouche, M. Loire, V. Simonet, R. Ballou, A. Stunault and A. Wildes, *Phys. Rev. B: Condens. Matter Mater. Phys.*, 2010, **82**, 100408.
97 H. Chu, C. J. Roh, J. O. Island, C. Li, S. Lee, J. Chen, J. G. Park, A. F. Young, J. S. Lee and D. Hsieh, *Phys. Rev. Lett.*, 2020, **124**, 027601.
98 Y. Dai, Y. Wang, S. Das, H. Xue, X. Bai, E. Hulkko, G. Zhang, X. Yang, Q. Dai and Z. Sun, *ACS Nano*, 2020, **14**, 8442–8448.
99 T. K. Fryett, K. L. Seyler, J. Zheng, C.-H. Liu, X. Xu and A. Majumdar, *2D Mater.*, 2016, **4**, 015031.
100 J. K. Day, M. H. Chung, Y. H. Lee and V. M. Menon, *Opt. Mater. Express*, 2016, **6**, 2360–2365.
101 X. T. Gan, C. Y. Zhao, S. Q. Hu, T. Wang, Y. Song, J. Li, Q. H. Zhao, W. Q. Jie and J. L. Zhao, *Light: Sci. Appl.*, 2018, **7**, 17126.
102 B. Jiang, Z. Hao, Y. Ji, Y. Hou, R. Yi, D. Mao, X. Gan and J. Zhao, *Light: Sci. Appl.*, 2020, **9**, 63.
103 K. Chen, X. Zhou, X. Cheng, R. Qiao, Y. Cheng, C. Liu, Y. Xie, W. Yu, F. Yao, Z. Sun, F. Wang, K. Liu and Z. Liu, *Nat. Photonics*, 2019, **13**, 754–759.
104 Y. Zuo, W. Yu, C. Liu, X. Cheng, R. Qiao, J. Liang, X. Zhou, J. Wang, M. Wu, Y. Zhao, P. Gao, S. Wu, Z. Sun, K. Liu, X. Bai and Z. Liu, *Nat. Nanotechnol.*, 2020, DOI: 10.1038/s41565-020-0770-x.
105 H. Hu, X. Yang, F. Zhai, D. Hu, R. Liu, K. Liu, Z. Sun and Q. Dai, *Nat. Commun.*, 2016, **7**, 12334.
106 H. Chen, V. Corboliou, A. S. Solntsev, D. Y. Choi, M. A. Vincenti, D. de Ceglia, C. de Angelis, Y. Lu and D. N. Neshev, *Light: Sci. Appl.*, 2017, **6**, e17060.
107 D. Sa, R. Valentí and C. Gros, *Eur. Phys. J. B*, 2000, **14**, 301–305.
108 B. B. Van Aken, J. P. Rivera, H. Schmid and M. Fiebig, *Nature*, 2007, **449**, 702–705.
109 W. Jin, E. Drueke, S. Li, A. Admasu, R. Owen, M. Day, K. Sun, S.-W. Cheong and L. Zhao, *Nat. Phys.*, 2019, **16**, 42–46.
110 D. H. Torchinsky, H. Chu, L. Zhao, N. B. Perkins, Y. Sizyuk, T. Qi, G. Cao and D. Hsieh, *Phys. Rev. Lett.*, 2015, **114**, 096404.
111 J. Liang, T. Tu, G. Chen, Y. Sun, R. Qiao, H. Ma, W. Yu, X. Zhou, C. Ma, P. Gao, H. Peng, K. Liu and D. Yu, *Adv. Mater.*, 2020, e2002831, DOI: 10.1002/adma.202002831.
112 Z. Ye, T. Cao, K. O'Brien, H. Zhu, X. Yin, Y. Wang, S. G. Louie and X. Zhang, *Nature*, 2014, **513**, 214–218.
113 J. Xiao, Z. Ye, Y. Wang, H. Zhu, Y. Wang and X. Zhang, *Light: Sci. Appl.*, 2015, **4**, e366–e366.
114 J. Cheng, D. Huang, T. Jiang, Y. Shan, Y. Li, S. Wu and W. T. Liu, *Opt. Lett.*, 2019, **44**, 2141–2144.
115 L. Du, J. Tang, J. Liang, M. Liao, Z. Jia, Q. Zhang, Y. Zhao, R. Yang, D. Shi, L. Gu, J. Xiang, K. Liu, Z. Sun and G. Zhang, *Research*, 2019, **2019**, 6494565.
116 X. Liu, J. Yi, Q. Li, S. Yang, W. Bao, C. Ropp, S. Lan, Y. Wang and X. Zhang, *Nano Lett.*, 2020, **20**, 1676–1685.
117 D. Hsieh, J. W. McIver, D. H. Torchinsky, D. R. Gardner, Y. S. Lee and N. Gedik, *Phys. Rev. Lett.*, 2011, **106**, 057401.
118 L. Wu, S. Patankar, T. Morimoto, N. L. Nair, E. Thewalt, A. Little, J. G. Analytis, J. E. Moore and J. Orenstein, *Nat. Phys.*, 2017, **13**, 350–355.
119 S. Patankar, L. Wu, B. Z. Lu, M. Rai, J. D. Tran, T. Morimoto, D. E. Parker, A. G. Grushin, N. L. Nair, J. G. Analytis, J. E. Moore, J. Orenstein and D. H. Torchinsky, *Phys. Rev. B*, 2018, **98**, 165113.
120 R. W. Boyd, *Nonlinear optics*, Academic Press, 2008, pp. 5–6.
121 N. W. Ashcroft, *Solid State Physics*, Holt, Rinehart and Winston, 1976, pp. 73–75.
122 R. W. Boyd, *Nonlinear Optics*, Academic Press, 2008, pp. 33–39.
123 P. Lu, J. Kim, J. Yang, H. Gao, J. Wu, D. Shao, B. Li, J. Sun, D. Akinwande, D. Xing and J. F. Liu, *Phys. Rev. B*, 2016, **94**, 224512.